Journal of the Optical Society of America A
OPTICS, IMAGE SCIENCE, AND VISION

Radiative transport and optical tomography with large datasets

MANABU MACHIDA,[1] GEORGE Y. PANASYUK,[2] ZHENG-MIN WANG,[3] VADIM A. MARKEL,[4] AND JOHN C. SCHOTLAND[1,5,*]

[1]Department of Mathematics, University of Michigan, Ann Arbor, Michigan 48109, USA
[2]Propulsion Directorate, Air Force Research Laboratory, Wright-Patterson Air Force Base, Ohio 45433, USA
[3]Department of Bioengineering, University of Pennsylvania, Philadelphia, Pennsylvania 19104, USA
[4]Aix-Marseille Université, CNRS, Centrale Marseille, Institut Fresnel UMR 7249, 130113 Marseille, France
[5]Department of Physics, University of Michigan, Ann Arbor, Michigan 48109, USA
*Corresponding author: schotland@umich.edu

Received 21 September 2015; revised 28 October 2015; accepted 16 November 2015; posted 11 December 2015 (Doc. ID 250385); published 10 March 2016

We consider the inverse problem of optical tomography in the radiative transport regime. We report numerical tests of a direct reconstruction method that is suitable for use with large datasets. Reconstructions of experimental data obtained from a noncontact optical tomography system are also reported.

OCIS codes: (170.6960) Tomography; (110.0113) Imaging through turbid media.

http://dx.doi.org/10.1364/JOSAA.33.000551

1. INTRODUCTION

The development of tools to probe the structure of highly scattering media such as clouds, colloids, and biological tissue is of fundamental interest and considerable applied importance. One such method, known as optical tomography (OT), is a biomedical imaging modality with unique capabilities to assess physiological function, such as blood volume and tissue oxygenation [1]. In a typical OT experiment, a material medium is illuminated by a narrow collimated beam and the light that propagates through the medium is collected by an array of detectors. In many instruments, the sources and detectors are coupled to the medium by means of optical fibers and the number of measurements which can be obtained varies from 10^2 – 10^5 source-detector pairs. More recently, *noncontact* imaging systems have been introduced, wherein a scanned beam and a lens-coupled CCD camera are employed to replace the aforementioned illumination and detection fiber-optics [2–4]. Using such a noncontact method, extremely large datasets of order 10^7 – 10^9 measurements can readily be acquired. The availability of such datasets has been shown to vastly improve the quality of images in OT [4–6].

The inverse problem of OT is to reconstruct the optical properties of a highly scattering medium from boundary measurements. The standard computational approach to this problem is to minimize a penalized least-squares functional [1,7–15]. Although such optimization methods are extremely flexible, they have very high computational cost and are not well suited to the large datasets of noncontact optical tomography. Direct reconstruction methods offer an alternative approach to optimization-based algorithms [16–23]. By direct reconstruction, we mean the use of inversion formulas and associated fast algorithms. Such formulas have been derived for particular experimental geometries, including those with planar boundaries. To date, these methods have been developed within the framework of the diffusion approximation (DA) to the radiative transport equation (RTE). We note that the DA is accurate when the energy density of the optical field varies slowly on the scale of the transport mean free path. The DA breaks down in optically thin layers, near boundaries and in strongly absorbing media, conditions that are frequently encountered in biomedical applications.

In this paper, we develop a direct reconstruction method for the inverse problem in the transport regime. The primary tools that we exploit are an integral equation formulation of the forward problem [24] and the recently derived plane-wave decomposition for the Green's function of the RTE [25–27]. Using this approach, we show that the *linearized* inverse problem can be formulated in terms of the inversion of a suitably defined Fourier–Laplace transform. We illustrate this result with numerical simulations and reconstructions of experimental data obtained from a noncontact OT system.

The remainder of this paper is organized as follows. In Section 2, we introduce the linearized forward problem within the accuracy of the Rytov approximation. This is followed in Section 3 by the derivation of the Fourier–Laplace inversion formula for the slab geometry. Numerically simulated

reconstructions are presented in Section 4. Reconstructions from experimental data are shown in Section 5. Our conclusions are presented in Section 6. The derivation of the Green's function for the RTE with reflecting boundary conditions is given in Appendix A.

2. FORWARD PROBLEM

A. Radiative Transport

The propagation of multiply scattered light in a volume Ω is taken to be governed by the RTE:

$$\hat{\mathbf{s}}\cdot\nabla I+(\mu_a(\mathbf{r})+\mu_s(\mathbf{r}))I=\mu_s(\mathbf{r})\int A(\hat{\mathbf{s}},\hat{\mathbf{s}}')I(\mathbf{r},\hat{\mathbf{s}}')\mathrm{d}^2s'+S(\mathbf{r},\hat{\mathbf{s}}). \tag{1}$$

Here, $I(\mathbf{r},\hat{\mathbf{s}})$ denotes the specific intensity at the point $\mathbf{r}$ in the direction $\hat{\mathbf{s}}$, S is the source, and μ_a and μ_s are the absorption and scattering coefficients of the medium. The phase function A is normalized so that $\int A(\hat{\mathbf{s}},\hat{\mathbf{s}}')\mathrm{d}^2s'=1$ for all $\hat{\mathbf{s}}$. The specific intensity is also assumed to obey the half-range boundary condition

$$I(\mathbf{r},\hat{\mathbf{s}}')=R(|\hat{\mathbf{s}}\cdot\hat{\mathbf{s}}'|)I(\mathbf{r},\hat{\mathbf{s}}),\qquad \hat{\mathbf{n}}\cdot\hat{\mathbf{s}}'<0\quad \text{on } \partial\Omega. \tag{2}$$

Here, R is the reflection coefficient, $\hat{\mathbf{n}}$ is the outward unit normal to $\partial\Omega$, and $\hat{\mathbf{s}}$ and $\hat{\mathbf{s}}'$ are the incident and reflected directions at the boundary, respectively. See Appendix A for further details.

We assume that the scattering coefficient μ_s is constant everywhere in the medium but the absorption coefficient μ_a varies with position. We thus decompose μ_a into a constant part $\bar{\mu}_a$ and a spatially varying part $\delta\mu_a$:

$$\mu_a(\mathbf{r})=\bar{\mu}_a+\delta\mu_a(\mathbf{r}). \tag{3}$$

The RTE (1) thus becomes

$$\hat{\mathbf{s}}\cdot\nabla I+\mu_t I+\delta\mu_a(\mathbf{r})I=\mu_s\int A(\hat{\mathbf{s}},\hat{\mathbf{s}}')I(\mathbf{r},\hat{\mathbf{s}}')\mathrm{d}^2s'+S, \tag{4}$$

where $\mu_t=\bar{\mu}_a+\mu_s$. The solution to Eq. (4) is given by

$$I(\mathbf{r},\hat{\mathbf{s}})=I_0(\mathbf{r},\hat{\mathbf{s}})-\int \mathrm{d}^3r'\mathrm{d}^2s'G(\mathbf{r},\hat{\mathbf{s}};\mathbf{r}',\hat{\mathbf{s}}')\delta\mu_a(\mathbf{r}')I(\mathbf{r}',\hat{\mathbf{s}}'). \tag{5}$$

Here, I_0 is the incident-specific intensity, defined as the solution to Eq. (1) with $\mu_a=\bar{\mu}_a$ obeying the boundary condition (2). The Green's function G satisfies the equation

$$\hat{\mathbf{s}}\cdot\nabla_{\mathbf{r}}G(\mathbf{r},\hat{\mathbf{s}};\mathbf{r}',\hat{\mathbf{s}}')+\mu_t G(\mathbf{r},\hat{\mathbf{s}};\mathbf{r}',\hat{\mathbf{s}}')= \tag{6}$$

$$\mu_s\int A(\hat{\mathbf{s}},\hat{\mathbf{s}}'')G(\mathbf{r},\hat{\mathbf{s}}'';\mathbf{r}',\hat{\mathbf{s}}')\mathrm{d}^2s''+\delta(\mathbf{r}-\mathbf{r}')\delta(\hat{\mathbf{s}}-\hat{\mathbf{s}}') \tag{7}$$

and obeys the boundary condition (2). Equation (5) is the analog of the Lippmann–Schwinger equation for the RTE. It can be linearized by the Rytov approximation [1]:

$$-\ln\left(\frac{I(\mathbf{r},\hat{\mathbf{s}})}{I_0(\mathbf{r},\hat{\mathbf{s}})}\right)=\frac{1}{I_0(\mathbf{r},\hat{\mathbf{s}})}\int \mathrm{d}^3r'\mathrm{d}^2s'G(\mathbf{r},\hat{\mathbf{s}};\mathbf{r}',\hat{\mathbf{s}}')\delta\mu_a(\mathbf{r}')I_0(\mathbf{r}',\hat{\mathbf{s}}'). \tag{8}$$

It will prove convenient to introduce the data function ϕ, which is defined by

$$\phi=-I_0\ln(I/I_0). \tag{9}$$

It follows from Eq. (8) that ϕ obeys the integral equation

$$\phi(\mathbf{r})=\int \mathrm{d}^3r'\mathrm{d}^2s'G(\mathbf{r},\hat{\mathbf{s}};\mathbf{r}',\hat{\mathbf{s}}')\delta\mu_a(\mathbf{r}')I_0(\mathbf{r}',\hat{\mathbf{s}}'). \tag{10}$$

B. Slab Geometry

For the remainder of this paper we consider a three-dimensional slab-shaped medium, as shown in Fig. 1. The incident field is taken to be generated by a point source oriented in the inward normal direction located on the $z=0$ plane. Thus $I_0=G(\mathbf{r},\hat{\mathbf{s}};\boldsymbol{\rho}_s,0,\hat{\mathbf{z}})$, where $\boldsymbol{\rho}_s$ is the transverse coordinate of the source. Light exiting the slab in the outward normal direction is collected by a point detector that is located on the plane $z=L$. The integral equation (10) thus becomes

$$\phi(\boldsymbol{\rho}_s,\boldsymbol{\rho}_d)=\int \mathrm{d}^3r\mathrm{d}^2sG(\boldsymbol{\rho}_d,L,\hat{\mathbf{z}};\mathbf{r},\hat{\mathbf{s}})G(\mathbf{r},\hat{\mathbf{s}};\boldsymbol{\rho}_s,0,-\hat{\mathbf{z}})\delta\mu_a(\mathbf{r}), \tag{11}$$

where $\boldsymbol{\rho}_d$ is the transverse coordinate of the detector.

To make further progress, we make use of the method of rotated reference frames to express the Green's function as an expansion in two-dimensional plane waves and spherical harmonics [25–27]. The details are presented in Appendix A, where it is shown that

$$G(\boldsymbol{r},\hat{\mathbf{s}};\boldsymbol{r}',\hat{\mathbf{s}}')=\int\frac{\mathrm{d}^2q}{(2\pi)^2}e^{-i\boldsymbol{q}\cdot(\boldsymbol{\rho}-\boldsymbol{\rho}')}\sum_{l=0}^{\infty}\sum_{m=-l}^{l}k_{lm}(\boldsymbol{q},z)Y_{lm}(\hat{\mathbf{s}})Y_{lm}^*(\hat{\mathbf{s}}'), \tag{12}$$

where $\mathbf{r}=(\boldsymbol{\rho},z)$ and k_{lm} is defined in Eq. (A19). Using this result, we find that Eq. (11) becomes

$$\phi(\boldsymbol{\rho}_s,\boldsymbol{\rho}_d)=\int \mathrm{d}^3r\int\frac{\mathrm{d}^2q_1}{(2\pi)^2}\int\frac{\mathrm{d}^2q_2}{(2\pi)^2}e^{i(\boldsymbol{q}_1-\boldsymbol{q}_2)\cdot\boldsymbol{\rho}}e^{-i(\boldsymbol{q}_1\cdot\boldsymbol{\rho}_s-\boldsymbol{q}_2\cdot\boldsymbol{\rho}_d)}\times\kappa(\boldsymbol{q}_1,\boldsymbol{q}_2,z)\delta\mu_a(\mathbf{r}), \tag{13}$$

where

$$\kappa(\boldsymbol{q}_1,\boldsymbol{q}_2,z)=\sum_{l=0}^{\infty}\sum_{m=-l}^{l}(-1)^m k_{lm}(\mathbf{q}_1,z)k_{lm}^*(\mathbf{q}_2,L-z). \tag{14}$$

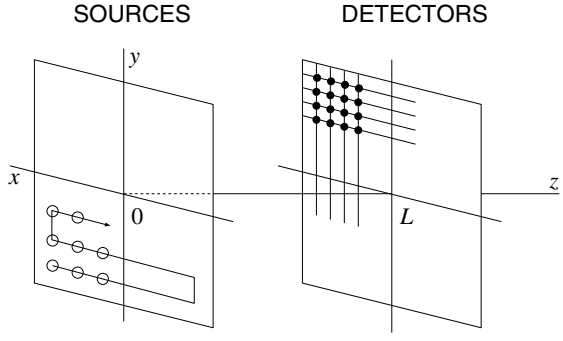

Fig. 1. Illustrating the slab geometry.

3. INVERSE PROBLEM

The inverse problem consists of recovering the absorption $\delta\mu_a$ from measurements of the data function ϕ. To proceed, we assume that the sources and detectors are placed on square lattices with lattice spacings h_s and h_d, respectively. The positions of the sources and detectors are given by

$$\boldsymbol{\rho}_s = h_s(n_{sx}\hat{\mathbf{x}} + n_{sy}\hat{\mathbf{y}}), \qquad \boldsymbol{\rho}_d = h_d(n_{dx}\hat{\mathbf{x}} + n_{dy}\hat{\mathbf{y}}), \tag{15}$$

where n_{sx}, n_{sy}, n_{dx}, and n_{dy} are integers. We introduce the Fourier transform of the data function:

$$\tilde{\phi}(\boldsymbol{q}_s, \boldsymbol{q}_d) = \sum_{\boldsymbol{\rho}_s,\boldsymbol{\rho}_d} e^{i(\boldsymbol{q}_s\cdot\boldsymbol{\rho}_s + \boldsymbol{q}_d\cdot\boldsymbol{\rho}_d)}\phi(\boldsymbol{\rho}_s, \boldsymbol{\rho}_d). \tag{16}$$

Here, the vectors $\boldsymbol{q}_s$ and $\boldsymbol{q}_d$ lie in the first Brillouin zone (FBZ) of the source and detector lattices:

$$-\frac{\pi}{h_s} \le q_s^{(x)}, q_s^{(y)} \le \frac{\pi}{h_s}, \qquad -\frac{\pi}{h_d} \le q_d^{(x)}, q_d^{(y)} \le \frac{\pi}{h_d}. \tag{17}$$

To compute the Fourier transform, we make use of Eq. (13) and the identity

$$\sum_{\boldsymbol{\rho}} e^{i\boldsymbol{q}\cdot\boldsymbol{\rho}} = \left(\frac{2\pi}{h}\right)^2 \sum_{\boldsymbol{v}} \delta(\boldsymbol{q} + \boldsymbol{v}), \tag{18}$$

where $\boldsymbol{v}$ denotes a reciprocal lattice vector and $\boldsymbol{q} \in [-\frac{\pi}{h}, \frac{\pi}{h}] \times [-\frac{\pi}{h}, \frac{\pi}{h}]$. We thus obtain

$$\tilde{\phi}(\boldsymbol{q}_s, \boldsymbol{q}_d) = \frac{1}{h_s^2 h_d^2} \sum_{\boldsymbol{v}_s,\boldsymbol{v}_d} \int \mathrm{d}z \kappa(\boldsymbol{q}_s + \boldsymbol{v}_s, -\boldsymbol{q}_d + \boldsymbol{v}_d, z) \times \widetilde{\delta\mu}_a(\boldsymbol{q}_s + \boldsymbol{q}_d + \boldsymbol{v}_s - \boldsymbol{v}_d, z), \tag{19}$$

where

$$\widetilde{\delta\mu}_a(\boldsymbol{q}, z) = \int \mathrm{d}^2\rho e^{i\boldsymbol{q}\cdot\boldsymbol{\rho}}\delta\mu_a(\boldsymbol{\rho}, z). \tag{20}$$

Next, we perform the change of variables,

$$\boldsymbol{q}_s = \frac{\boldsymbol{q}}{2} + \boldsymbol{p}, \qquad \boldsymbol{q}_d = \frac{\boldsymbol{q}}{2} - \boldsymbol{p}, \tag{21}$$

where $\boldsymbol{q}_s$ and $\boldsymbol{q}_d$ are two-dimensional vectors. We also assume that $\delta\mu_a$ is transversely band-limited to the FBZs of the source-detector lattices (corresponding to the band limit $\min\{2\pi/h_s, 2\pi/h_d\}$) and therefore put $\boldsymbol{v}_s = 0$ and $\boldsymbol{v}_d = 0$ in Eq. (19), which thus becomes

$$\Phi(\boldsymbol{q}, \boldsymbol{p}) = \int_0^L K(\boldsymbol{q}, \boldsymbol{p}, z)\widetilde{\delta\mu}_a(\boldsymbol{q}, z)\mathrm{d}z, \tag{22}$$

where

$$\Phi(\boldsymbol{q}, \boldsymbol{p}) = h_s^2 h_d^2 \tilde{\phi}\left(\frac{\boldsymbol{q}}{2} + \boldsymbol{p}, \frac{\boldsymbol{q}}{2} - \boldsymbol{p}\right), \tag{23}$$

$$K(\boldsymbol{q}, \boldsymbol{p}, z) = \kappa\left(\boldsymbol{p} + \frac{\boldsymbol{q}}{2}, \boldsymbol{p} - \frac{\boldsymbol{q}}{2}, z\right). \tag{24}$$

For fixed $\boldsymbol{q}$, Eq. (22) defines a system of one-dimensional integral equations for the Fourier transform $\widetilde{\delta\mu}_a$. Following the general approach of [23], we construct the pseudoinverse solution of Eq. (22) and perform an inverse Fourier transform to obtain the inversion formula:

$$\delta\mu_a(\boldsymbol{\rho}, z) = \int_{\mathrm{FBZ}} \frac{\mathrm{d}^2 q}{(2\pi)^2} e^{-i\boldsymbol{q}\cdot\boldsymbol{\rho}} \sum_{\nu} \frac{R(\sigma_\nu(\boldsymbol{q}))}{\sigma_\nu^2(\boldsymbol{q})} \sum_{\boldsymbol{p},\boldsymbol{p}'} \langle f_\nu(\boldsymbol{q})|\boldsymbol{p}\rangle \times K^*(\boldsymbol{q}, \boldsymbol{p}', z)\langle \boldsymbol{p}'|f_\nu(\boldsymbol{q})\rangle \Phi(\boldsymbol{q}, \boldsymbol{p}). \tag{25}$$

Here, f_ν and σ_ν are the singular functions and singular values of the matrix M,

$$\sum_{\boldsymbol{p}'} \langle \boldsymbol{p}|M(\boldsymbol{q})|\boldsymbol{p}'\rangle\langle \boldsymbol{p}'|f_\nu(\boldsymbol{q})\rangle = \sigma_\nu^2(\boldsymbol{q})\langle \boldsymbol{p}|f_\nu(\boldsymbol{q})\rangle, \tag{26}$$

where M is defined by

$$\langle \boldsymbol{p}|M(\boldsymbol{q})|\boldsymbol{p}'\rangle = \int_0^L K(\boldsymbol{q}, \boldsymbol{p}, z)K^*(\boldsymbol{q}, \boldsymbol{p}', z)\mathrm{d}z. \tag{27}$$

The regularizer R is introduced to limit the effect of small singular values. Common choices of R include the Tikhonov regularizer $R(\sigma) = \sigma^2/(\sigma^2 + \epsilon)$ or the step function $R(\sigma) = \theta(\sigma - \epsilon)$, where $\epsilon > 0$. In our computations, both approaches give similar results.

4. NUMERICAL SIMULATIONS

In this section we report the results of numerical reconstructions from simulated forward data. The medium to be reconstructed consists of a set of five point absorbers, as shown in Fig. 2. The absorbers are assumed to have the same scattering coefficients and phase functions as the medium in which they are embedded, but have different absorption coefficients. The absorption coefficient $\delta\mu_a$ is given by

$$\delta\mu_a(\mathbf{r}) = \ell^{*2} \sum_{i=1}^{5} \delta(\mathbf{r} - \mathbf{r}_i), \tag{28}$$

where the positions of the absorbers are $(x_1, y_1, z_1) = (-4\ell^*, 2\ell^*, z_0 - \ell^*)$, $(x_2, y_2, z_2) = (-2\ell^*, 4\ell^*, z_0 - \ell^*)$, $(x_3, y_3, z_3) = (0, 0, z_0)$, $(x_4, y_4, z_4) = (2\ell^*, -4\ell^*, z_0 + \ell^*)$, and $(x_5, y_5, z_5) = (4\ell^*, -2\ell^*, z_0 + \ell^*)$. The optical properties of the background medium are taken to be

$$\bar{\mu}_a = 0.05\ \mathrm{cm}^{-1}, \qquad \mu_s = 100\ \mathrm{cm}^{-1}, \qquad g = 0.9. \tag{29}$$

Note that $\ell^* = 1.00$ mm in this case. The above values are typical for biological tissues in the near-IR spectral range. The data function Φ is calculated according to Eq. (22) for a sample with prescribed $\delta\mu_a$. Gaussian noise with zero mean and a standard deviation of 1% of the average signal is added to the data function Φ for each numerical experiment. Reconstructions of

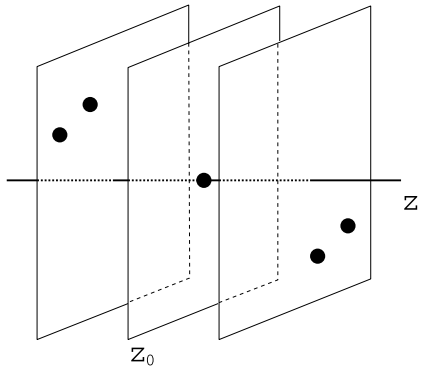

Fig. 2. Illustrating the set of five point absorbers.

$\delta\mu_a$ are calculated from Eq. (25) using the step function regularizer. The sum over l in the Green's function (12) is truncated at $l = l_{\max} = 9$.

The source and detector positions are given by Eq. (15) with $-N_s \le n_{sx}, n_{sy} \le N_s$ and $-N_d \le n_{dx}, n_{dy} \le N_d$. We also set $N_d = 120$ and $N_s = 120 h_d/h_s$. The wave vectors $\boldsymbol{q}$ and $\boldsymbol{p}$ are discretized as

$$\begin{aligned} \boldsymbol{q} &= \tfrac{2\pi}{h_d(2N_{\mathrm{FBZ}}+1)}(j_x\hat{\mathbf{x}} + j_y\hat{\mathbf{y}}), \quad -N_q \le j_x, j_y \le N_q, \\ \boldsymbol{p} &= \tfrac{2\pi}{h_d(2N_{\mathrm{FBZ}}+1)}(k_x\hat{\mathbf{x}} + k_y\hat{\mathbf{y}}), \quad 0 \le k_x, k_y \le N_p - 1, \end{aligned} \tag{30}$$

where N_{FBZ} is the number of points in the FBZ. We take N_q and N_p to be much smaller than N_{FBZ} to control numerical stability at high frequencies. We have found that $N_{\mathrm{FBZ}} = 120$, $N_q = 28$, and $N_p = 7$ are suitable choices. Finally, we note that numerical integration over z in Eq. (27) is carried out using Simpson's rule, with discretionzation $z_j = j(L - 2\ell^*)/N_z + \ell^*$ $(j = 0, 1, \ldots, N_z)$. For $L = 10\ell^*$ and $6\ell^*$ we take N_z to be 160 and 80, respectively.

A. Results

Reconstructions of $\delta\mu_a$ are shown in Figs. 3 and 4. Results are shown for two different slab thicknesses $L = 6\ell^*, 10\ell^*$. The source and detector lattice spacings are $h_s = 0.2\ell^*$ and $h_d = 0.1\ell^*$, respectively. In Fig. 3, we take $L = 10\ell^*$ and $z_0 = 5\ell^*$ in panel (a) and $L = 6\ell^*$ and $z_0 = 3\ell^*$ in panel (b). The regularization parameter is set to be $\varepsilon/\sqrt{\ell^*} = 10^{-6}$ for (a) and $\varepsilon/\sqrt{\ell^*} = 10^{-5}$ for (b). We see that the absorber is clearly reconstructed in both panels. We will define the resolution as the full width at half-maximum (FWHM) of the point spread function of the central absorber. Thus the resolution is approximately $2.0\ell^*$ in (a) and $1.5\ell^*$ in (b).

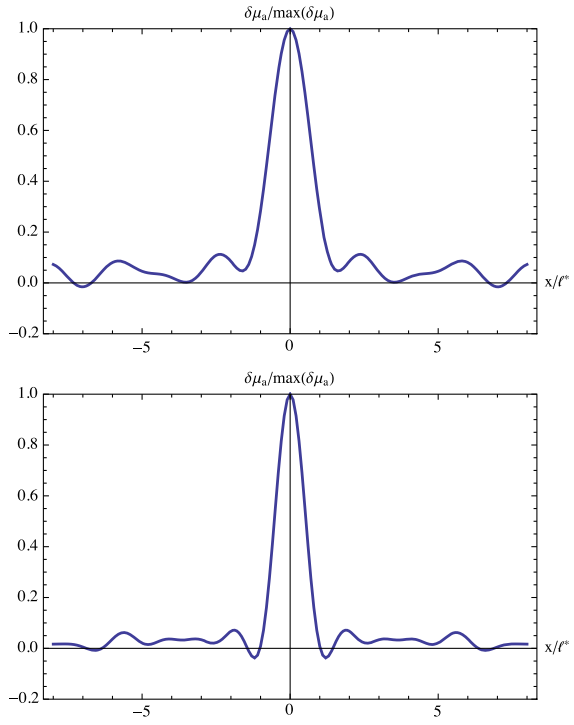

Fig. 3. Reconstructed $\delta\mu_a(x, y = 0, z = z_0)/\max[\delta\mu_a(x, 0, z_0)]$ are shown as a function of x/ℓ^*. The following cases are considered: $L = 10\ell^*$ and $z_0 = 5\ell^*$ (top) and $L = 6\ell^*$ and $z_0 = 3\ell^*$ (bottom).

B. Computational Complexity

The reconstructed images are obtained in 90 s using a four-cpu parallel machine of 1.3 GHz Itanium-2 processors. The most computationally expensive part of the reconstruction is the calculation of the kernel $K(\boldsymbol{q}, \boldsymbol{p}, z)$, which is obtained from k_{lm}. To compute k_{lm}, the Wigner function d^l_{mM} and $f^{(\pm)}_{Mn}$ must be calculated. For each $q(0 < q \le q_{\max})$, the construction of d^l_{mM} requires $O((l_{\max}+1)(l_{\max}+2)(l_{\max}+3))$ floating point operations and the calculation of $f^{(\pm)}_{Mn}$ requires $O((l_{\max}+1)^6)$ floating point operations. Therefore, when q is approximated by n_q discrete points, the computation of k_{lm} requires $O(N_z n_q l^8_{\max})$ floating point operations. Thus the computation of K requires $O(N_q^2 N_p^2 N_z l^2_{\max})$ floating point operations.

5. EXPERIMENTAL RESULTS

A. Experimental Setup

We have tested the reconstruction algorithm with experimental data using a previously described noncontact OT system [4]. The source is a continuous-wave stabilized diode laser operating at a wavelength of 785 nm with an output power of 6 mW. The sample chamber is a rectangular box, constructed of clear acrylic, of depth 1 cm with square faces of area 15 cm × 15 cm. The chamber is filled with a scattering medium in which the objects to be imaged are placed. The medium consists of a 1% solution of Intralipid in water. The beam is scanned by a pair of mirrors on one face of the sample and the transmitted beam is imaged onto a CCD.

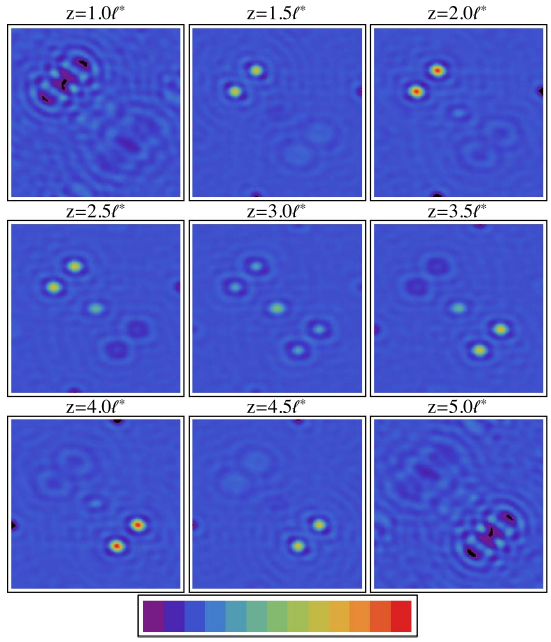

Fig. 4. Tomographic reconstruction of $\delta\mu_a$ for five point absorbers in a slab with $L = 6\ell^*$ and for $z_0 = L/2$. The function shown by the color scale is $\delta\mu_a(\mathbf{r})/\max_{\mathbf{r}}[\delta\mu_a(\mathbf{r})]$. The field of view in each panel is $16\ell^* \times 16\ell^*$.

A tomographic dataset is acquired by raster scanning the beam over a 29×29 square lattice with a lattice spacing of 3.21 mm. This yields 841 source positions within a 9 cm × 9 cm area centered on the optical axis. For each source, a 397×397 pixel region of interest is read out from the CCD. This results in 157,609 detectors arranged in a square lattice with an effective lattice spacing equivalent to 0.36 mm. Thus a dataset of 1.3×10^8 source-detector pairs is acquired.

B. Two Rods

In this section, we show the reconstruction of a pair of black metal rods. The rods have a diameter of 3 mm and are suspended in the midplane of the sample chamber. The optical properties of the background medium are

$$\bar{\mu}_a = 0.02\ \text{cm}^{-1}, \qquad \mu_s = 20\ \text{cm}^{-1}, \qquad g = 0.65,$$
$$k = 0.02 h_d^{-1}, \qquad \ell = 20 h_d, \tag{31}$$

where $k = \sqrt{c\mu_a/D}$ and $h_d = 0.36$ mm is the lattice spacing on the detector plane. These parameters yield a transport mean free path of $\ell^* = 1.4$ mm.

Initially, we set the separation of the rods to be 3 mm and take $l_{\max} = 9$. In Fig. 5, tomographic images are displayed with a slice separation of 1 mm. It can be seen that in the central slice, which is equidistant from the source and the detector planes, that the rods are well resolved. The shallower and deeper slices show that the rods remain well resolved but with a smaller diameter, as expected. Figure 6 shows a plot of the reconstruction along the line passing through the centers of both rods in the central slice. The distance between the peaks is 5.8 mm, which slightly underestimates the center-to-center separation of the rods. The FWHM of the peaks is 2.3 mm, which underestimates the diameter of the rods.

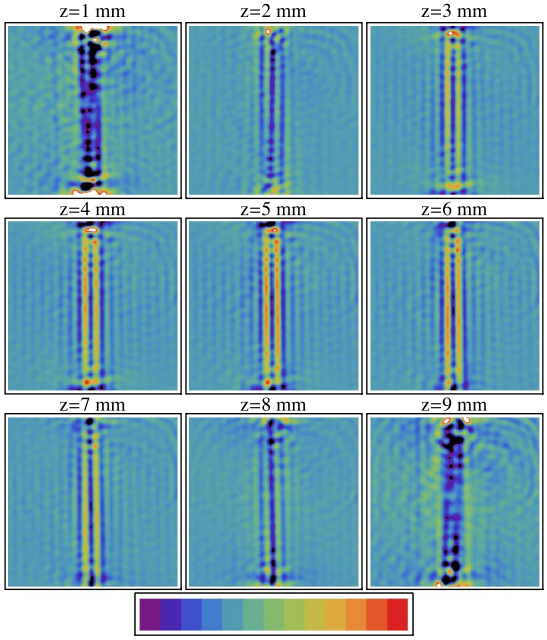

Fig. 5. Reconstructions of two rods with 3 mm spacing. The field of view is 6 cm × 6 cm. The number above each panel shows the distance from the source plane.

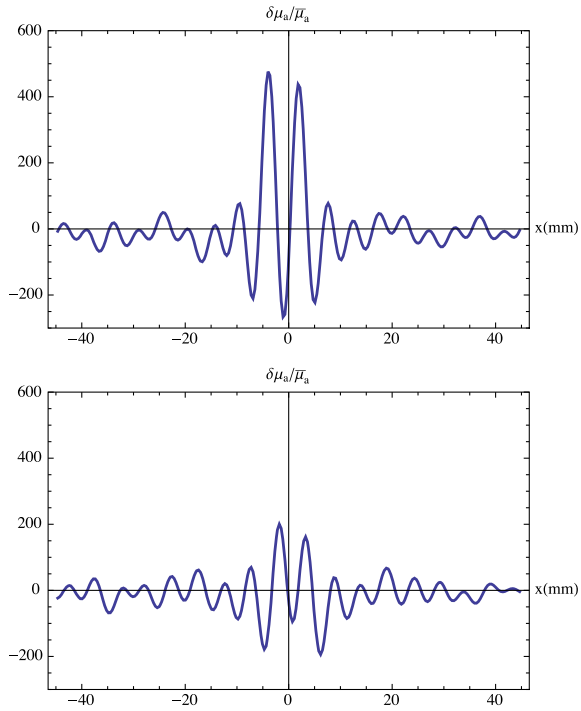

Fig. 6. Reconstructed $\delta\mu_a/\bar{\mu}_a$ of the metal rods with (top) 3 mm spacing and (bottom) 2 mm spacing along the x-axis in the central plane at $y = 0$ and $z = 5$ mm.

In a second experiment, we set the separation between the rods to be 2 mm. In this case the reconstructed image is poorly resolved. The lower panel in Fig. 6 shows a two-dimensional plot in the central slice. It is important to note that the reconstructed contrast is not expected to be quantitative owing to the strong absorption in the interior of the metal rods. However, as previously noted, the shape of the rods is recovered well.

C. Lemon and Lotus Root Slices

In a final set of experiments, a lemon or lotus root slice of thickness approximately 4 mm is placed in the center of the sample chamber. The background medium consists of 0.7% Intralipid plus 0.07% India ink, with optical properties

$$\bar{\mu}_a = 0.4\ \text{cm}^{-1}, \qquad \mu_s = 20\ \text{cm}^{-1}, \qquad g = 0.65,$$
$$k = 0.13 h_d^{-1}, \qquad \ell = 20 h_d. \tag{32}$$

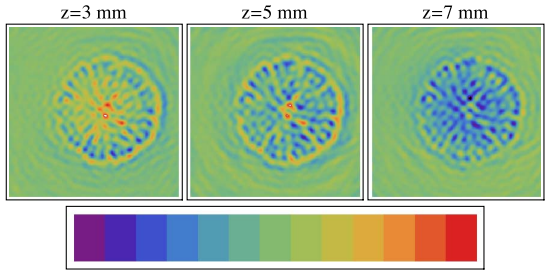

Fig. 7. RTE reconstructions of a lemon slice. The field of view is 9 cm × 9 cm. The number above each panel shows the distance from the source plane.

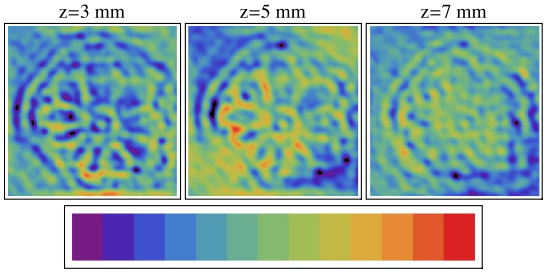

Fig. 8. RTE reconstructions of a lotus root slice. The field of view is 9 cm × 9 cm. The number above each panel shows the distance from the source plane.

Reconstructions of the lemon and lotus root are shown in Figs. 7 and 8, respectively. A number of structural features of the lemon, including the endocarp, mesocarp, central column and septa, are readily visualized. Likewise, root tubes of varying diameter are observable.

6. DISCUSSION

In summary, we have investigated the inverse problem of optical tomography in the radiative transport regime. We have developed and tested a fast image reconstruction algorithm that is applicable to the large datasets of noncontact optical tomography. Our results are illustrated by numerical simulations and reconstructions from experimental data in model systems.

We conclude with several remarks. First, the spatial resolution of the reconstructed images in numerical simulations is clearly superior to that obtained in experiments. There are a number of contributing factors that explain this finding. These include the finite size of the source and detector grids, the presence of shot noise in the detected light, and noise in the CCD array. We have also not accounted for systematic errors associated with nonidealities in the optical system, such as reflections from the lens surface. Second, the reconstructions we have performed are carried out within a linearization of the RTE. It may be expected that a nonlinear reconstruction may overcome some of the above limitations, particularly with respect to quantitative recovery of the absorption. One possible approach to this problem is inversion of the Born series, which has been carried out for the case of the DA [20–22]. Inversion of the linearized forward problem is the first step in this procedure, which can be carried out by the method developed herein. Finally, detailed comparisons of our results with reconstructions carried out within the diffusion approximation will be the subject of future research. It will be important to understand the role of systematic errors as well as experimental noise in controlling the resolution of reconstructed images. Some discussion of these points has been provided in [4,5].

APPENDIX A: GREEN'S FUNCTION FOR THE RTE

In this appendix, we outline the calculation of the Green's function for the RTE using the method of rotated reference frames (MRRF). The MRRF was described in [25–27]. Here we summarize the necessary results for the case of the slab geometry with reflecting boundaries. We note that the MRRF has also been extended to the case of reflecting boundaries in the half-space geometry [28].

We begin by noting that the Green's function for the RTE in the slab geometry satisfies the equation

$$(\hat{\mathbf{s}}\cdot\nabla+\mu_t)G(\boldsymbol{r},\hat{\mathbf{s}};\boldsymbol{\rho}_0,0,\hat{\mathbf{z}}) = \mu_s\int A(\hat{\mathbf{s}},\hat{\mathbf{s}}')G(\boldsymbol{r},\hat{\mathbf{s}}';\boldsymbol{\rho}_0,0,\hat{\mathbf{z}})\mathrm{d}^2s' + \delta(\boldsymbol{\rho}-\boldsymbol{\rho}_0)\delta(z)\delta(\hat{\mathbf{s}}-\hat{\mathbf{z}}), \tag{A1}$$

together with the boundary conditions

$$G(\boldsymbol{r},\hat{\mathbf{s}}_r;\boldsymbol{\rho}_0,0,\hat{\mathbf{z}}) = R(|\hat{\mathbf{s}}_i\cdot\hat{\mathbf{z}}|)G(\boldsymbol{r},\hat{\mathbf{s}}_i;\boldsymbol{\rho}_0,0,\hat{\mathbf{z}}),\quad \hat{\mathbf{n}}\cdot\hat{\mathbf{s}}<0,\qquad z=0,L. \tag{A2}$$

The reflection coefficient R is given by [29–34]

$$R(x) = \begin{cases} \frac{1}{2}\left[\left(\frac{x-nx_0}{x+nx_0}\right)^2+\left(\frac{x_0-nx}{x_0+nx}\right)^2\right] & x\geq x_c,\\ 1 & x<x_c, \end{cases} \tag{A3}$$

where $x_0=\sqrt{1-n^2(1-x^2)}$, $x_c=\sqrt{n^2-1}/n$, and n is the index of refraction in the slab walls (see Fig. 9). We assume that the phase function A is given by

$$A(\hat{\mathbf{s}},\hat{\mathbf{s}}') = \sum_{l=0}^{l_{\max}}\sum_{m=-l}^{l} A_l Y_{lm}(\hat{\mathbf{s}})Y_{lm}^*(\hat{\mathbf{s}}'), \tag{A4}$$

where $A_0=1$, $A_1=g\in[0,1)$, and $A_l\in[0,1)$ $(l=2,3,\ldots)$. We adopt the Henyey–Greenstein model [35], and set

$$A_l = g^l,\qquad l=0,1,2,\ldots. \tag{A5}$$

In the MRRF [25–28], the specific intensity is given as a superposition of eigenmodes $I_\mu^{(+)}$ and $I_\mu^{(-)}$, where

$$I_\mu^{(+)}(\boldsymbol{r},\hat{\mathbf{s}};\boldsymbol{q}) = e^{i\boldsymbol{q}\cdot\boldsymbol{\rho}-Q_\mu(q)z}\sum_{l=0}^{l_{\max}}\sum_{m=-l}^{l}\frac{(-1)^m}{\sqrt{\sigma_l}}e^{-im\varphi_{\hat{q}}}\langle l|\phi_\mu\rangle \times d_{mM}^l[i\tau(q\lambda_\mu)]Y_{lm}(\hat{\mathbf{s}}), \tag{A6}$$

$$I_\mu^{(-)}(\boldsymbol{r},\hat{\mathbf{s}};\boldsymbol{q}) = e^{i\boldsymbol{q}\cdot\boldsymbol{\rho}+Q_\mu(q)z}\sum_{l=0}^{l_{\max}}\sum_{m=-l}^{l}\frac{(-1)^l}{\sqrt{\sigma_l}}e^{-im\varphi_{\hat{q}}}\langle l|\phi_\mu\rangle \times d_{m,-M}^l[i\tau(q\lambda_\mu)]Y_{lm}(\hat{\mathbf{s}}), \tag{A7}$$

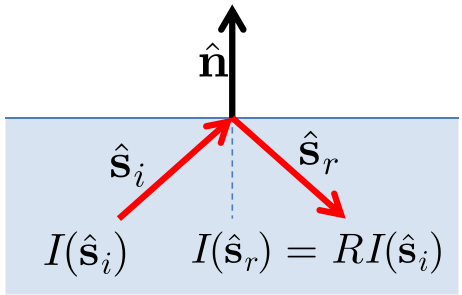

Fig. 9. Illustrating the reflecting boundary condition.

where

$$Q_\mu(q) = \sqrt{q^2 + 1/\lambda_\mu^2}. \tag{A8}$$

Here, $\lambda_n(M)$ and $|\phi_n(M)\rangle$ are eigenvalues and eigenvectors of matrix $B(M)$ defined by

$$B(M)_{ll'} = \sqrt{\frac{l^2 - M^2}{(4l^2 - 1)\sigma_{l-1}\sigma_l}}\delta_{l',l-1} + \sqrt{\frac{(l+1)^2 - M^2}{[4(l+1)^2 - 1]\sigma_l\sigma_{l+1}}}\delta_{l',l+1}, \tag{A9}$$

where $\sigma_l = \bar{\mu}_a + \mu_s(1 - g^l)$, l, $l' = |M|, |M| + 1, \ldots, l_{\max}$, and $M = 0, \pm 1, \pm 2, \ldots$. Note that we make use of a multi-index $\mu = (M, n)$, which runs over the set $\{(M, n)|\lambda_n(M) > 0\}$. The d^l_{mM} are analytically continued Wigner's d-functions, which can be recursively computed [25]. The Green's function can be expressed as

$$G(\boldsymbol{r}, \hat{\mathbf{s}}; \boldsymbol{\rho}_0, 0, \hat{\mathbf{z}}) = \sum_\mu \int \frac{\mathrm{d}^2 q}{(2\pi)^2} e^{-i\boldsymbol{q}\cdot\boldsymbol{\rho}_0}[f^{(+)}_\mu(q; n)I^{(+)}_\mu(\boldsymbol{r}, \hat{\mathbf{s}}; \boldsymbol{q}) + f^{(-)}_\mu(q; n)e^{-Q_\mu(q)L}I^{(-)}_\mu(\boldsymbol{r}, \hat{\mathbf{s}}; \boldsymbol{q})]. \tag{A10}$$

The coefficients $f^{(+)}_\mu(q; n)$ and $f^{(-)}_\mu(q; n)$ are determined by the boundary conditions and are solutions to the linear system

$$\begin{pmatrix} \mathcal{M}^{(++)}(q) & \mathcal{M}^{(+-)}(q) \\ \mathcal{M}^{(-+)}(q) & \mathcal{M}^{(--)}(q) \end{pmatrix} \begin{pmatrix} f^{(+)}(q; n) \\ f^{(-)}(q; n) \end{pmatrix} = \begin{pmatrix} v^{(+)} \\ v^{(-)} \end{pmatrix}, \tag{A11}$$

where $M \geq 0$, $m \geq 0$, $l = m + 1, m + 3, \ldots$,

$$v^{(+)}_{lm} = \delta_{m0}\sum_{l'} \mathcal{B}^0_{ll'}(\infty)\sqrt{\frac{2l' + 1}{4\pi}}, \qquad v^{(-)}_{lm} = 0, \tag{A12}$$

and

$$\mathcal{M}^{(++)}_{lm,Mn} = \sum_{l'} c^{l'}_{lm,Mn}, \quad \mathcal{M}^{(--)}_{lm,Mn} = (-1)^{M+m}\mathcal{M}^{(++)}_{lm,Mn}, \tag{A13}$$

$$\mathcal{M}^{(+-)}_{lm,Mn} = (-1)^{M+m}\mathcal{M}^{(-+)}_{lm,Mn}, \quad \mathcal{M}^{(-+)}_{lm,Mn} = e^{-Q_\mu(q)L}\sum_{l'}(-1)^{l'} c^{l'}_{lm,Mn}, \tag{A14}$$

$$c^{l'}_{lm,Mn} = [\mathcal{B}^m_{ll'}(\infty) - (-1)^{l'+m}\mathcal{B}^m_{ll'}(n)]\frac{1}{\sqrt{\sigma_{l'}}}\langle l'|\phi_\mu\rangle \times \{d^{l'}_{mM}[i\tau(q\lambda_\mu)] + (1 - \delta_{M0})(-1)^M d^{l'}_{m-M}[i\tau(q\lambda_\mu)]\}. \tag{A15}$$

Here, $\mathcal{B}^m_{ll'}(n)$ is given by

$$\mathcal{B}^m_{ll'}(n) = \frac{1}{2}\sqrt{\frac{(2l + 1)(2l' + 1)(l - m)!(l' - m)!}{(l + m)!(l' + m)!}} \tag{A16}$$

$$\times \int_0^1 \mathrm{d}x P^m_l(x)P^m_{l'}(x)R_n(x). \tag{A17}$$

We note that $\mathcal{B}^{-m}_{ll'}(n) = \mathcal{B}^m_{ll'}(n)$, and $\mathcal{B}^m_{ll'}(\infty)$ is defined by $\mathcal{B}^m_{ll'}(n)$ with $R_n(x) \equiv 1$. We also note that $f^{(\pm)}_{-Mn}(q; n) = (-1)^M f^{(\pm)}_{Mn}(q; n)$. Finally, the Green's function in the slab geometry is obtained as [25]

$$G(\boldsymbol{r}, \hat{\mathbf{s}}; \boldsymbol{\rho}_0, 0, \hat{\mathbf{z}}) \simeq \int \frac{\mathrm{d}^2 q}{(2\pi)^2} e^{-i\boldsymbol{q}\cdot(\boldsymbol{\rho} - \boldsymbol{\rho}_0)} \sum_{l=0}^{l_{\max}} \sum_{m=-l}^{l} Y_{lm}(\hat{\mathbf{s}})i^m k_{lm}(\boldsymbol{q}, z), \tag{A18}$$

where the functions $k_{lm}(\boldsymbol{q}, z)$ are given by

$$k_{lm}(\boldsymbol{q}, z) = (-i)^m e^{-im\varphi_q} \sum_{M \geq 0, n} \frac{\langle l|\phi_n(M)\rangle}{\sqrt{\sigma_l}} \times [e^{-Q_{Mn}(q)z} f^{(+)}_{Mn}(q; n) + (-1)^{l+m+M} e^{-Q_{Mn}(q)(L-z)} f^{(-)}_{Mn}(q; n)] \times [d^l_{mM}[i\tau(q\lambda_n(M))] + (1 - \delta_{M0})(-1)^M d^l_{m,-M}[i\tau(q\lambda_n(M))]], \tag{A19}$$

with $\varphi_{\boldsymbol{q}}$ the angle of $\boldsymbol{q}$.

Funding. National Institutes of Health (NIH) (P41-RR002305, R01EB004832); National Science Foundation (NSF) (DMS-0554100, DMS-1108969).

REFERENCES

1. S. R. Arridge and J. C. Schotland, "Optical tomography: forward and inverse problems," Inverse Probl. **25**, 123010 (2009).
2. G. Turner, G. Zacharakis, A. Soubret, J. Ripoll, and V. Ntziachristos, "Complete-angle projection diffuse optical tomography by use of early photons," Opt. Lett. **30**, 409–411 (2005).
3. R. Schulz, J. Ripoll, and V. Ntziachristos, "Noncontact optical tomography of turbid media," Opt. Lett. **28**, 1701–1703 (2003).
4. Z.-M. Wang, G. Panasyuk, V. Markel, and J. C. Schotland, "Experimental demonstration of an analytic method for image reconstruction in optical tomography with large data sets," Opt. Lett. **30**, 3338–3340 (2005).
5. S. D. Konecky, G. Y. Panasyuk, K. Lee, V. Markel, A. G. Yodh, and J. C. Schotland, "Imaging complex structures with diffuse light," Opt. Express **16**, 5048–5060 (2008).
6. S. Konecky, A. Mahzar, D. Cuccia, A. Durkin, J. Schotland, and B. Tromberg, "Quantitative optical tomography of subsurface heterogeneities using spatially modulated structured light," Opt. Express **17**, 14780–14790 (2009).
7. G. Bal, "Inverse transport theory and applications," Inverse Probl. **25**, 053001 (2009).
8. G. S. Abdoulaev, K. Ren, and A. H. Hielscher, "Optical tomography as a PDE-constrained optimization problem," Inverse Probl. **21**, 1507–1530 (2005).
9. H. K. Kim and A. H. Hielscher, "A PDE-constrained SQP algorithm for optical tomography based on the frequency-domain equation of radiative transfer," Inverse Probl. **25**, 015010 (2009).
10. K. Ren, G. Bal, and A. H. Hielscher, "Frequency domain optical tomography based on the equation of radiative transfer," SIAM J. Sci. Comput. **28**, 1463–1489 (2006).
11. O. Dorn, "A transport-backtransport method for optical tomography," Inverse Probl. **14**, 1107–1130 (1998).
12. P. Gonzalez-Rodriguez and A. D. Kim, "Reflectance optical tomography in epithelial tissues," Inverse Probl. **25**, 015001 (2009).
13. A. Joshi, J. C. Rasmussen, E. M. Sevick-Muraca, T. A. Wareing, and J. McGhee, "Radiative transport-based frequency-domain fluorescence tomography," Phys. Med. Biol. **53**, 2069–2088 (2008).
14. A. D. Kim, C. Hayakawa, and V. Venugopalan, "Estimating tissue optical properties using the Born approximation of the transport equation," Opt. Lett. **31**, 1088–1090 (2006).

15. T. Tarvainen, M. Vaukhonen, and S. R. Arridge, "Gauss-Newton reconstruction method for optical tomography using the finite element solution of the radiative transfer equation," J. Quant. Spectrosc. Radiat. Transfer **109**, 2767–2778 (2008).
16. J. Schotland, "Continuous-wave diffusion imaging," J. Opt. Soc. Am. A **14**, 275–279 (1997).
17. J. Schotland and V. Markel, "Inverse scattering with diffusing waves," J. Opt. Soc. Am. A **18**, 2767–2777 (2001).
18. V. Markel and J. Schotland, "Effects of sampling and limited data in optical tomography," Appl. Phys. Lett. **81**, 1180–1182 (2002).
19. V. Markel, V. Mital, and J. Schotland, "Inverse problem in optical diffusion tomography. III inversion formulas and singular value decomposition," J. Opt. Soc. Am. A **20**, 890–902 (2003).
20. V. Markel, J. O'sullivan, and J. Schotland, "Inverse problem in optical diffusion tomography. IV nonlinear inversion formulas," J. Opt. Soc. Am. A **20**, 903–912 (2003).
21. S. Moskow and J. Schotland, "Convergence and stability of the inverse scattering series for diffuse waves," Inverse Probl. **24**, 065005 (2008).
22. M. Moskow and J. Schotland, "Numerical studies of the inverse born series for diffuse waves," Inverse Probl. **25**, 095007 (2009).
23. V. A. Markel and J. C. Schotland, "Symmetries, inversion formulas, and image reconstruction for optical tomography," Phys. Rev. E **70**, 056616 (2004).
24. J. C. Schotland and V. A. Markel, "Fourier-Laplace structure of the inverse scattering problem for the radiative transport equation," Inv. Probl. Imaging **1**, 181–188 (2007).
25. M. Machida, G. Y. Panasyuk, J. C. Schotland, and V. A. Markel, "The Green's function for the radiative transport equation in the slab geometry," J. Phys. A **43**, 065402 (2010).
26. V. A. Markel, "Modified spherical harmonics method for solving the radiative transport equation," Waves Random Medium **14**, L13–L19 (2004).
27. G. Panasyuk, J. C. Schotland, and V. A. Markel, "Radiative transport equation in rotated reference frames," J. Phys. A **39**, 115–137 (2006).
28. A. Liemert and A. Kienle, "Light transport in three-dimensional semi-infinite scattering media," J. Opt. Soc. Am. A **29**, 1475–1481 (2012).
29. A. D. Kim, "A boundary integral method to compute Green's functions for the radiative transport equation," Waves Random Complex Medium **15**, 17–42 (2005).
30. J. S. Cassell and M. M. R. Williams, "Radiation transport and internal reflection in a sphere," J. Quant. Spectrosc. Radiat. Transfer **101**, 16–28 (2006).
31. J. S. Cassell and M. M. R. Williams, "Radiation transport and internal reflection in a two region, turbid sphere," J. Quant. Spectrosc. Radiat. Transfer **104**, 400–427 (2007).
32. R. D. M. Garcia, C. E. Siewert, and A. M. Yacout, "On the use of Fresnel boundary and interface conditions in radiative-transfer calculations for multilayered media," J. Quant. Spectrosc. Radiat. Transfer **109**, 752–769 (2008).
33. R. Aronson, "Boundary conditions for diffusion of light," J. Opt. Soc. Am. A **12**, 2532–2539 (1995).
34. M. M. R. Williams, "On an integral equation arising in the transport of radiation through a slab involving internal reflection," Eur. Phys. J. B **47**, 291–293 (2005).
35. L. G. Henyey and J. L. Greenstein, "Diffuse radiation in the galaxy," Astrophys. J. **93**, 70–84 (1941).